

1           **On the Relationships between Low-Frequency**  
2           **Variations of Earth's Rotation and Equatorial**  
3           **Atmospheric Angular Momentum**

4                           **T. W. Hadi<sup>1</sup>, F. R. Fajary<sup>1</sup>, S. Yoden<sup>2</sup>**

5                           <sup>1</sup>Atmospheric Science Research Group, Bandung Institute of Technology, Indonesia

6                           <sup>2</sup>Institute for Liberal Arts and Sciences, Kyoto University, Japan

7           **Key Points:**

- 8           • A positive trend in the mass term of atmospheric angular momentum correlates  
9           with observed increasing rate of the Earth's rotation
- 10          • The conditions of accelerating Earth's rotation agree with a positive trend in the  
11          motion term of equatorial atmospheric angular momentum
- 12          • Interrelationship between low-frequency modulations of Earth's rotation and at-  
13          mospheric angular momentum is evidenced

---

Corresponding author: Tri W. Hadi, [tri.wahyu@itb.ac.id](mailto:tri.wahyu@itb.ac.id)

14 **Abstract**

15 This work mainly concerns low-frequency variations of Atmospheric Angular Momen-  
 16 tum (AAM), emphasizing the role of the equatorial region and its relationships with the  
 17 length of day (*LOD*), whose observed time series indicate an accelerating Earth’s rota-  
 18 tion over the last several decades. We applied bivariate and trivariate Empirical Mode  
 19 Decomposition methods to extract coherent nonstationary signals from the monthly time  
 20 series of *LOD* and the two components of AAM, i.e., the mass term  $M_{\Omega}$  and the mo-  
 21 tion term  $M_r$ . It is found that, over the global domain, a decreasing trend of *LOD* dur-  
 22 ing the last five decades correlates with an increasing trend in  $M_{\Omega}$ , whereas the trend  
 23 in  $M_r$  is negligible. However, there is a significantly positive trend in  $M_r$  of the equa-  
 24 torial lower troposphere (1000 to 700 hPa), which can be associated with a larger trans-  
 25 fer of eastward momentum due to the accelerating Earth. Further analyses of spatio-temporal  
 26 distribution of  $M_r$  anomalies suggest that, at multidecadal time scales, residual changes  
 27 in the motion term of AAM across the globe tend to be in balance. The long-term pos-  
 28 itive trend in  $M_{\Omega}$ , which is dominant over the equatorial latitude belt, is most likely at-  
 29 tributed to prolonged effects of the global increase in surface pressure from the mid-1970s  
 30 until the 1990s. Low-frequency variations of *LOD* are also found to have a high corre-  
 31 lation with the Atlantic Meridional Oscillation index. Our results suggest that long-term  
 32 changes in the Earth’s rotation rate are partially attributable to the atmospheric and  
 33 oceanic variability of comparable time scales.

34 **1 Introduction**

35 The relationships between the variation of Earth’s rotation rate — measured as changes  
 36 in the length of day (*LOD*) — and climate have been a long-standing geophysical prob-  
 37 lem. The fact that the Earth has been spinning faster for the last several decades has  
 38 also sparked attention from wider research communities and raised concerns about the  
 39 possible effects of global warming. Numerous studies have previously confirmed that *LOD*  
 40 excitations at intraseasonal, seasonal, to interannual time scales are associated with global  
 41 atmospheric angular momentum (AAM) variations due to various climatic phenomena  
 42 (Madden, 1987; Feldstein, 1999; Abarca-del Rio et al., 2000; Aoyama & Naito, 2000; Eg-  
 43 ger et al., 2007). However, attributions and physical mechanisms responsible for *LOD*  
 44 variations at decadal or longer time scales are still a subject of scientific debates (e.g.,  
 45 Lambeck & Hopgood, 1982; Duhau, 2006; Barlyaeva et al., 2014; Huang et al., 2001).

46 The linkage between *LOD* and global atmospheric circulation has been deduced  
 47 from the angular momentum conservation principle (Starr, 1948; Oort, 1989), but Gong  
 48 et al. (2019) found that increasing global AAM in recent decades cannot explain the neg-  
 49 ative trend of *LOD*. Huang et al. (2001) have previously pointed out from climate sim-  
 50 ulations under global warming conditions that a positive trend in AAM should corre-  
 51 spond to an increase in *LOD* by +0.3 to +0.5 ms in a century. In these works, the neg-  
 52 ative trends in *LOD* have been attributed to non-atmospheric sources, i.e., core-mantel  
 53 (Gong et al., 2019) and postglacial (Huang et al., 2001) processes.

54 Thus, attributing low-frequency variations of *LOD* to climatic processes is still a  
 55 challenging problem, but Zotov et al. (2016) pointed out a significant correlation between  
 56 global temperature anomaly and *LOD* variations at a multidecadal time scale. This and  
 57 some other studies suggest that dynamical interaction between climatic processes and  
 58 Earth’s rotation may also occur at decadal or longer time scales, which should be im-  
 59 printed in the characteristics of the low-frequency variations of AAM. However, previ-  
 60 ous studies on the relationships between AAM and *LOD* variations may not have ex-  
 61 amined the following aspects in detail:

- 62 1. The total AAM is composed of two components expressed as  $M_a = M_\Omega + M_r$   
 63 (e.g., Oort, 1989). The  $M_\Omega$  term (herein, also referred to as the mass term) is the  
 64 AAM component due to the Earth’s solid body rotation, whereas the  $M_r$  term is  
 65 due to atmospheric motion relative to the rotating Earth (hence, the motion term).  
 66 It is important to note that  $M_\Omega$  and  $M_r$  may undergo different time evolution as  
 67 shown from the results of global warming simulations (Huang et al., 2001), which  
 68 implies that correlations between  $M_\Omega$ ,  $M_r$ , and *LOD* need to be analyzed sepa-  
 69 rately.
- 70 2. The AAM in the equatorial region has unique characteristics because  $M_\Omega$  is large  
 71 due to a relatively larger radius of the rotational plane. In addition, the zonal winds  
 72 are predominantly easterly, so that  $M_r$  is on the average negative. The Earth’s  
 73 angular momentum conservation principle implies that the Earth’s surface con-  
 74 tinuously transfers absolute angular momentum to the atmosphere along the equa-  
 75 torial latitudes with surface easterlies (Starr, 1948). The excess angular momen-  
 76 tum in the equatorial atmosphere is then transported poleward mainly by weather  
 77 processes in the troposphere to be deposited back to the Earth in midlatitudes with

78 surface westerlies (e.g., Weickmann & Sardeshmukh, 1994). The existence of Quasi-  
 79 Biennial Oscillation (QBO) in the equatorial stratosphere also affects  $M_r$  varia-  
 80 tions (e.g., Salstein, 2015; Match & Fueglistaler, 2019).

- 81 3. Transient eddy momentum flux induced by phenomena like Madden-Julian oscil-  
 82 lation (MJO) and El Niño southern oscillation (ENSO) in the tropical/equatorial  
 83 region may leave a residual contribution to the mean climate state (Huang et al.,  
 84 2001; Lee, 1999). However, MJO, ENSO, and other similar phenomena occur with  
 85 irregular or quasi-regular patterns in time and space so that nonstationary vari-  
 86 ations likely characterize any residual signal.

87 The main objective of this study is to investigate low-frequency variations of global  
 88 AAM and their relationships with  $LOD$ , with emphasis on the role of zonal-mean wind  
 89 variations in the troposphere over the equatorial region. Technically, low-frequency com-  
 90 ponents in a single time-series data can be extracted using several methods. The most  
 91 common one is using a low-pass filter such as Butterworth filter design (e.g., Fajary et  
 92 al., 2019). However, a novel approach is needed to extract coherent low-frequency sig-  
 93 nals from two or more nonstationary time series simultaneously. A data analysis method  
 94 that can deal with nonstationary signals is empirical mode decomposition (EMD), which  
 95 extracts intrinsic (natural) signals from an observed time series (Wu et al., 2007). Some  
 96 implementations of EMD methods have been extended to multivariate inputs (e.g., Wu  
 97 et al., 2016; Thirumalaisamy & Ansell, 2018). The application of multivariate EMD method  
 98 allows us to analyze the correlations among  $M_\Omega$ ,  $M_r$ , and  $LOD$  simultaneously yet sep-  
 99 arately. Thus, besides a specific analysis of low-frequency variations in the equatorial AAM,  
 100 we also emphasize the application of the multivariate EMD method as a novelty in the  
 101 present work.

## 102 **2 Materials and Methods**

### 103 **2.1 Data**

104 In this investigation, we mainly analyze globally gridded monthly zonal winds from  
 105 NCEP R1 reanalysis dataset (NCEP/NWS/NOAA/U.S. Department of Commerce, 1994;  
 106 Kalnay et al., 1996) because, among others, it has the longest record spanning from 1948  
 107 to the present. We notice that there are biases in the NCEP data when compared to MERRA-  
 108 2 reanalysis, which is considered as a benchmark for accuracy (Fujiwara et al., 2017),

109 but we assume that long-term AAM variations are still well represented in the former  
 110 dataset (Paek & Huang, 2012; Gong et al., 2019).

111 The LOD data, representing the Earth’s rotation rate, was obtained from the In-  
 112 ternational Earth Rotation and Reference Systems Service (IERS) as daily time series  
 113 started from 1 January 1962 (IERS Earth Orientation Centre, 2020; Bizouard et al., 2019).  
 114 In this work, we also use several climate indices accessible from the National Oceanic and  
 115 Atmospheric Administration (NOAA) Physical Science Laboratory (PSL) website (PSL/NOAA,  
 116 2020). Herein, we mainly use monthly-mean time series; daily data are converted into  
 117 monthly-mean time series through simple averaging. Any special treatment or data pro-  
 118 cessing is explained in the text wherever needed for clarity. Additional results from our  
 119 data processing can be found in the Supporting Information (SI).

## 120 2.2 Calculation of the AAM

121 The derivation of mathematical formulae to calculate AAM has been comprehen-  
 122 sively discussed in previous works (Barnes et al., 1983; Salstein et al., 1993), and the glob-  
 123 ally integrated motion term can be expressed by (e.g., Gong et al., 2019; Huang et al.,  
 124 2001)

$$M_r = \frac{a^3}{g} \int_p \int_\lambda \int_\phi u \cos^2 \phi \, d\phi \, d\lambda \, dp, \quad (1)$$

125 whereas mass term is given by

$$M_\Omega = \frac{a^4 \Omega}{g} \int_\lambda \int_\phi p_s \cos^3 \phi \, d\phi \, d\lambda. \quad (2)$$

126 In these equations,  $u$  and  $p_s$  are zonal wind and surface pressure, respectively. For  $M_r$ ,  
 127 the integration is carried out with respect to latitude  $\phi$ , longitude  $\lambda$ , and pressure  $p$ , whereas  
 128  $M_\Omega$  is the horizontal integrals over the globe at the surface. The other parameters. i.e.  
 129  $\Omega$ ,  $a$ , and  $g$  are Earth’s angular velocity, Earth’s radius, and gravity acceleration assumed  
 130 constant. There are two schemes for  $M_\Omega$  calculation, i.e. with and without inverted baro-  
 131 metric (IB) assumptions (Barnes et al., 1983; Salstein et al., 1993). In this case, we only  
 132 applied a non-inverted barometric (non-IB) scheme in the evaluation of (2). We validated  
 133 our results against AAM data provided by NOAA, which are also accessible from the  
 134 aforementioned IERS’s website. Although some discrepancies exists, comparisons of out-  
 135 put variables show a linear correlation with regression coefficients close to unity (not shown).

136

### 2.3 Definition of The Equatorial Belt

137

138

139

140

141

142

143

144

145

146

147

In the following analyses, we differentiate the AAM variations contributed by the equatorial region from the global domain. Among quite a few literatures, Grimes (1951) define the equatorial belt by the latitudes between 15°S and 15°N where it is assumed that the Coriolis force ceases to predominate. Herein, we defines the equatorial belt by the latitudes between 20°S and 20°N where the climatology of AAM is predominantly negative as shown in Fig. S1(a) in SI. Although all-year negative AAM is mainly confined within the 15° latitudes, we consider to include transitional or buffer zones, where AAM may fluctuate between negative and positive values seasonally (Fig. S1(b)), so that our definition of the equatorial belt is wider than that of Grimes (1951) by 5°. Transition zones between the equatorial and mid-latitude regions are marked by a relatively rapid decrease of  $M_{\Omega}$  with latitudes (Fig. S1(c)).

148

149

150

151

152

153

154

155

156

157

158

To our knowledge, there is no strict distinction between the definitions of equatorial and tropical belts, but it should be common sense to assume that the former is a sub-region of the latter. The tropical belt itself has several definitions with latitudinal extents that may surpass 20° in both hemispheres depending on the metrics being used (Birner et al., 2014; Davis & Rosenlof, 2012). Egger and Hoinka (2005) used 27° latitudes to mark the boundaries between tropical and midlatitude regions when analyzing the characteristics of AAM. On the other hand, Huang et al. (2001) examined tropical contribution on changes in AAM due to projected increase in sea surface temperature (SST) under global warming conditions by averaging data between the latitudes of 13°S and 13°N. In the study, it is remarked that their index is not sensitive to the choice of the averaging domain.

159

### 2.4 Identification of Coherent Low-Frequency Variabilities

160

161

162

We employed the EMD method to analyze time-series data presumed to contain nonstationary low-frequency signals. A univariate EMD analysis of a time series  $f(t)$  will result in its decomposition into several intrinsic mode functions, *IMFs*, i.e.,

$$f(t) = \sum_{n=1}^N IMF\#n(t) + \mathfrak{R}(t), \quad (3)$$

163

164

where  $\mathfrak{R}(t)$  is the residual, the discrepancy between the summed *IMFs* and original time series. The EMD is a completely "data-driven" method because it does not assume any

165 a priori basis function so that detection of spurious signals can be avoided (Wu et al.,  
 166 2007). However, the maximum number of *IMFs*,  $N$  in Eq. (3), is determined through  
 167 an iterative process with results that may be sensitive to small variations in the dataset.  
 168 Consequently, each *IMF* obtained from EMD analysis of different time series may have  
 169 different physical meanings and must be more carefully interpreted.

170 Various EMD techniques to analyze univariate and multivariate time series have  
 171 also been developed and applied to climate data (e.g. Wu et al., 2016). In this work, we  
 172 adopt the multivariate EMD method developed by Thirumalaisamy and Ansell (2018).  
 173 By applying a multivariate EMD analysis, we assume that physically meaningful *IMFs*  
 174 can be effectively rendered from correlated nonstationary time series. Matlab<sup>®</sup> codes to  
 175 implement the multivariate EMD analysis have been provided by Thirumalaisamy (2020),  
 176 which includes codes to perform simultaneous EMD with input up to 16 (channel) time  
 177 series of one, two, and three spatial dimensions. For our purposes, however, it is suffi-  
 178 cient to apply only bivariate and trivariate one-dimensional (either in latitude or pres-  
 179 sure) EMD, whereby up to two or three time-series can be analyzed simultaneously in  
 180 one code execution on a regular personal computer.

### 181 **3 Results**

#### 182 **3.1 Correlations between *LOD* and Global AAM**

183 This subsection first discusses the correlation between *LOD* and two AAM com-  
 184 ponents, i.e.,  $M_r$  and  $M_\Omega$ , computed over the global domain. From Fig. 1, we can see  
 185 that the time series of *LOD* exhibit a decreasing trend from the 1970s to the present with  
 186 superimposed oscillatory signals of multidecadal and shorter periods. It is also clear that  
 187  $M_\Omega$  is two orders of magnitude larger than  $M_r$ , but the standard deviation of  $M_r$  is one  
 188 order larger than that of  $M_\Omega$ . However, it should be noted that  $M_r$  is always globally  
 189 positive despite negative values in the equatorial region (further discussed below). In gen-  
 190 eral, correlations between *LOD* and total AAM  $M_a$  are not visually discernible except  
 191 for some concurrent spikes in certain years, such as that of 1982/83 El Niño. In addi-  
 192 tion, marked interdecadal variations can be seen in the time series of  $M_\Omega$ , especially be-  
 193 tween the 1950s and 1980s.

194 Correlations among parameters in Fig. 1 are more intuitively depicted as scatter  
 195 plots in Fig. 2. There is a positive correlation between  $M_r$  and *LOD* with a drift due

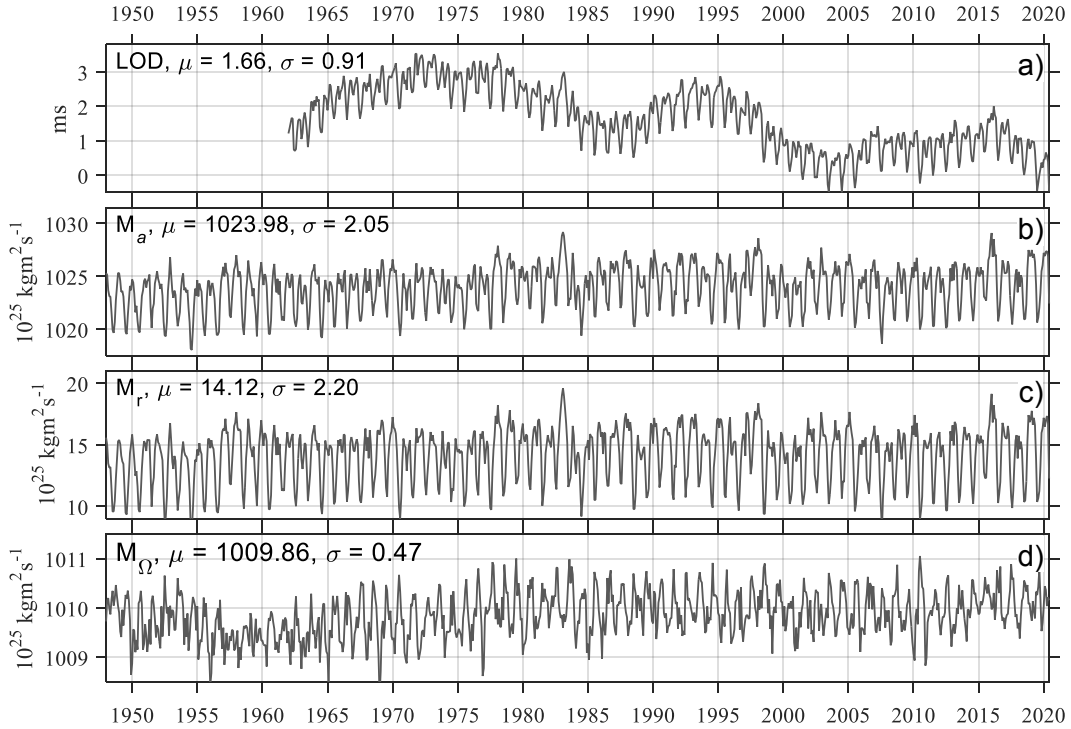


**Figure 1.** Time series of (a)  $LOD$ , (b)  $M_a$ , (c)  $M_r$ , and (d)  $M_\Omega$  of the global AAM (see text for explanation) at a monthly time interval. Units, means  $\mu$ , and standard deviations  $\sigma$ , of the time series are also indicated in the plots.

196 to the long-term decreasing trend of  $LOD$ , whereas  $M_\Omega$  is negatively correlated with the  
 197 other two parameters. We can see that the correlation patterns change over time by in-  
 198 specting the color-coded time information, signifying a non-stationary relationship be-  
 199 tween compared parameters. The power spectral densities in Fig. 2(d) show that all pa-  
 200 rameters have strong and well-aligned annual and semiannual signals. Marked peaks are  
 201 also identified at QBO (2.4-year) and ENSO (5.0-year) periods. Signals with longer pe-  
 202 riods are red-noise contaminated, and their peaks occur at different frequency bands.

203 We further investigate the correlations between  $LOD$ ,  $M_r$ , and  $M_\Omega$  by applying  
 204 trivariate EMD analysis on the three time-series. Because all data have a very different  
 205 range of values, each of the parameters is normalized as  $\tilde{x} = (x - \mu_x) / \sigma_x$  where  $\mu_x$  and  
 206  $\sigma_x$  are the mean and standard deviation of  $x$ . We found that the EMD analyses are also  
 207 sensitive to the choice of window size, which is determined as a function of the distance  
 208 between extrema in the signal (Thirumalaisamy & Ansell, 2018). In this case, we have  
 209 chosen a window size equal to a maximum allowable value of 7 for all EMD analysis. Re-

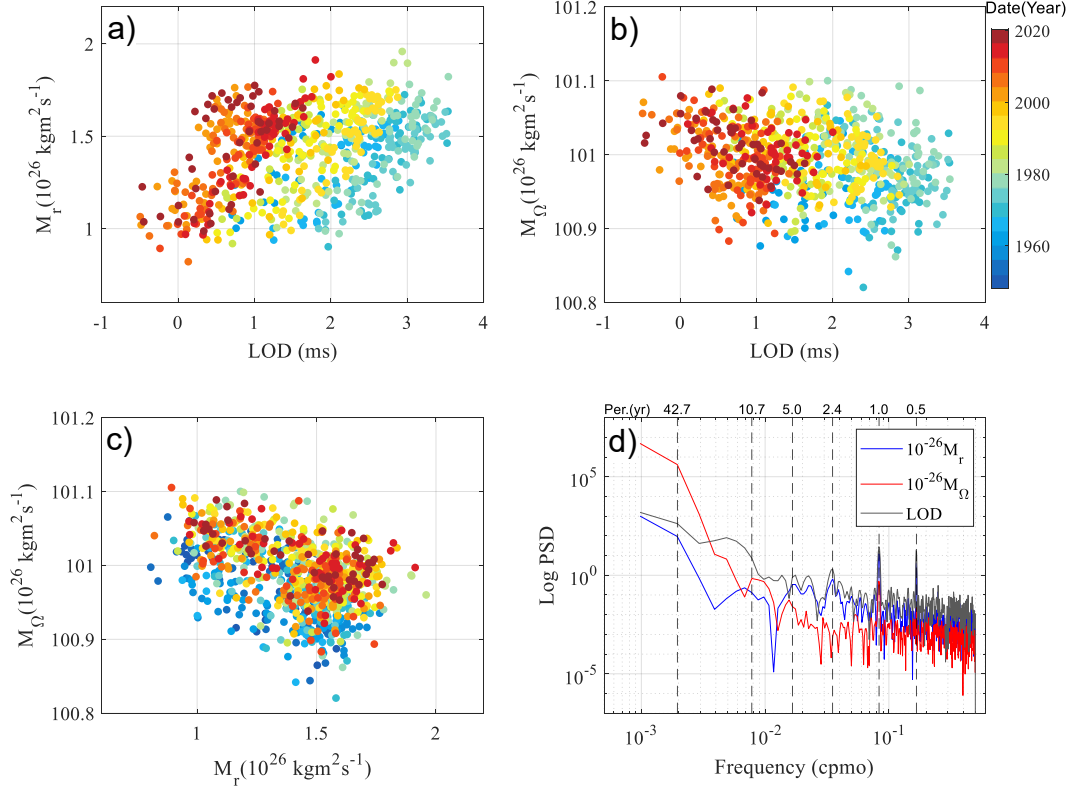


**Figure 2.** Scatter plots between parameters in Fig. 1 ((a) to (c)) and the corresponding Fourier power spectral densities (PSDs) in (d). Color codes are used to show time from the year 1948 to 2020. Values of  $M_r$  and  $M_\Omega$  are multiplied by  $10^{-26}$  prior to Fourier spectral computation.

210 results of the EMD analysis are shown in Fig. 3 as scatter plots of the *IMFs*. In addition,  
 211 to identify dominant periods in the decomposed signals, we also computed the cross power  
 212 spectral density (CPSD)  $P_{xy}$  and Spearman’s linear correlation coefficient  $r$ . The period  
 213 associated with maximum CPSD is determined as the period  $T_{xy}$  of two correlated sig-  
 214 nals given in a time unit of month (abbreviated as ”mo”). It should be noted that *IMFs*  
 215 #1 and #2 mainly contain signals of sub-annual variations and are not shown in Fig.  
 216 3.

217 Consistent with the spectral analysis in Fig. 2, we can see that the strongest co-  
 218 herent signals are those of annual variation. However, there are two modes of annual vari-  
 219 ability represented by *IMF*#3 and *IMF*#4. Discontinuities (clustering of data) in *IMF*#3  
 220 indicate the influence of strong seasonal patterns of midlatitude regions (see e.g., Sal-  
 221 stein, 2015), whereas smoother *IMF*#4 seems to characterize the contribution of trop-

222 ical/equatorial region. Note that  $M_r$  and  $M_\Omega$  are negatively correlated ( $r=-0.86$ ) for *IMF#3*,  
 223 while those are not much correlated ( $r=-0.38$ ) for *IMF#4*. It can also be seen that  $M_r$   
 224 has a relatively stronger linear correlation with *LOD*, up to QBO (28 mo) time scale as  
 225 indicated by the *IMF#5*. On the other hand, correlations between  $M_\Omega$  and *LOD*, as  
 226 well as  $M_r$ , are much weaker except for *IMF#3*. The results of EMD analysis clearly  
 227 show that correlations between the three parameters become nonstationary at time scales  
 228 of about 32 mo ( $\approx 2.7$  yr) and longer, especially when  $M_\Omega$  is involved. In this EMD anal-  
 229 ysis, the three signals can be decomposed up to *IMF#9*, but *IMF#8* is extremely weak  
 230 and difficult to interpret.

231 We are particularly interested in *IMF#9* that represents signals with multidecadal  
 232 time scales. Detailed temporal variations of *IMF#9* are shown in Fig. 4 along with the  
 233 residuals, which are obtained by subtracting the summed *IMFs* from the original time  
 234 series as defined by Eq. (3). In this case, the residual component  $\mathfrak{R}(t)$  is a function with  
 235 less than three detectable extrema and considered a non-oscillatory signal. Figure 4(a)  
 236 clearly shows that the *LOD* contains relatively large oscillatory signals with periods of  
 237 around 20 years, while  $M_r$  and  $M_\Omega$  exhibit less well-defined oscillations at this time scale.  
 238 It is of interest to note that variations in  $M_\Omega$  show a relatively consistent phase against  
 239 *LOD* with about five-year lag in the occurrences of local maxima. On the contrary,  $M_r$   
 240 variations have changed from out-of-phase, prior to the 1980s, to more in-phase after the  
 241 1990s. This explains the zero correlation coefficient between *IMF#9* of *LOD* and  $M_r$ ,  
 242 as shown in Figs. 3 and 4(a).

243 More comparable variations are depicted by the residuals of *LOD* and  $M_\Omega$  in Fig.  
 244 4(b) where opposite long-term trends that dominate over weak fluctuations can be seen.  
 245 The correlation coefficient computed from the time series of *LOD* and  $M_\Omega$  in Fig. 4(b)  
 246 is -0.72. On the other hand, the residual of  $M_r$  does not indicate a significant trend over  
 247 the last five decades. These results are interesting because the AAM variations are ba-  
 248 sically more characterized by  $M_r$  rather than  $M_\Omega$ , even under projected global warm-  
 249 ing conditions (e.g. Huang et al., 2001). Moreover, multidecadal variations of  $M_r$  and  
 250  $M_\Omega$  in Fig. 4(a) are positively correlated (see, *IMFs#9* in Fig. 3, bottom right with  $r=0.57$ )  
 251 in contrast to the negative correlations that characterize the annual variations in *IMFs*  
 252 #3 and #4. It is also of interest to note that such a positive correlation also character-  
 253 izes *IMFs* #6 and #7 with apparent contributions of ENSO and other variations of longer  
 254 time scales. Considering that  $M_\Omega$  is a function of  $\cos^3 \phi$  in Eq. (2), the equatorial re-

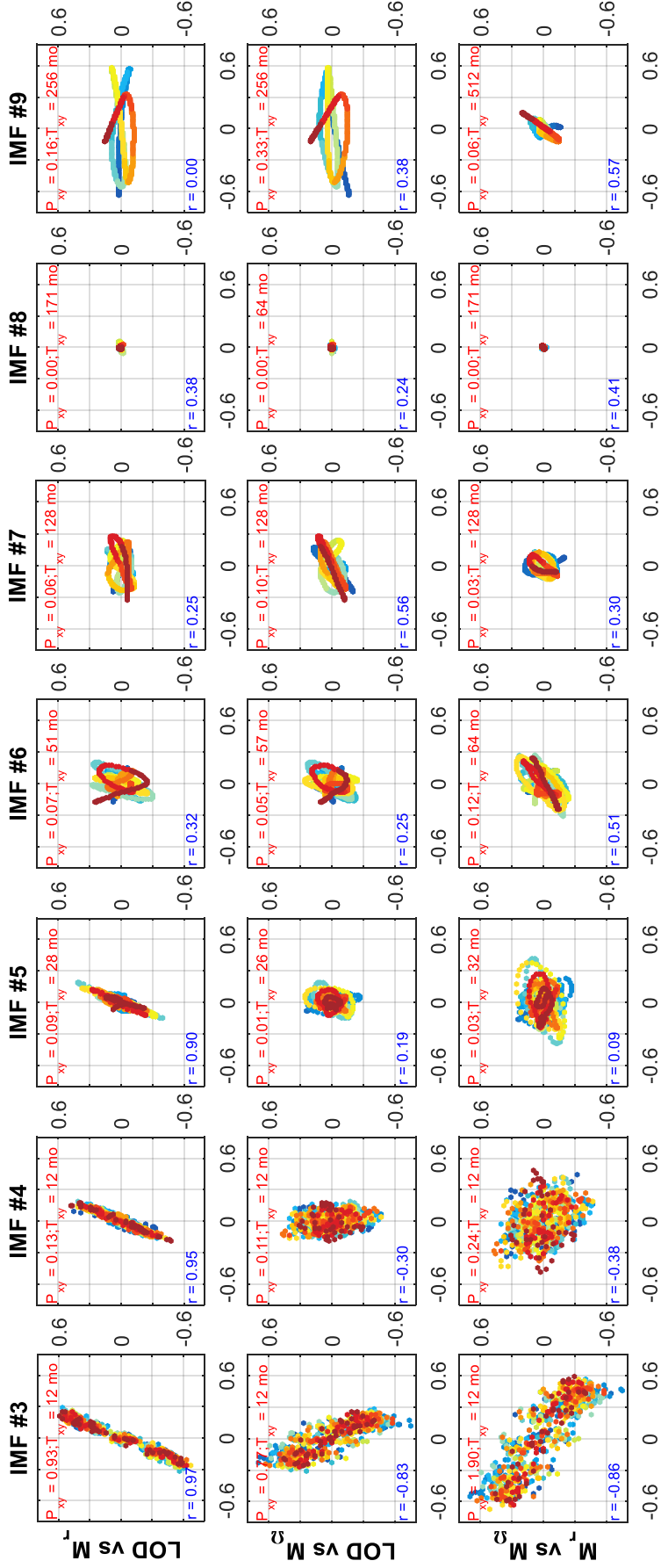


**Figure 3.** Scatter plots between *IMFs* resulted from trivariate EMD analysis of normalized  $M_r$ ,  $M_\Omega$ , and  $LOD$  time series. Spearman's correlation coefficients ( $r$  printed in blue) and maximum cross power spectral density (CPSD) along with the corresponding period ( $P_{xy}$  and  $T_{xy}$  printed in red) are also shown in each panel.

255 gion should significantly contribute to these low-frequency variations. Thus, it is nec-  
 256 essary to analyze the spatio-temporal variations of  $M_\Omega$  and  $M_r$  in more detail, partic-  
 257 ularly to clarify the role of the equatorial region.

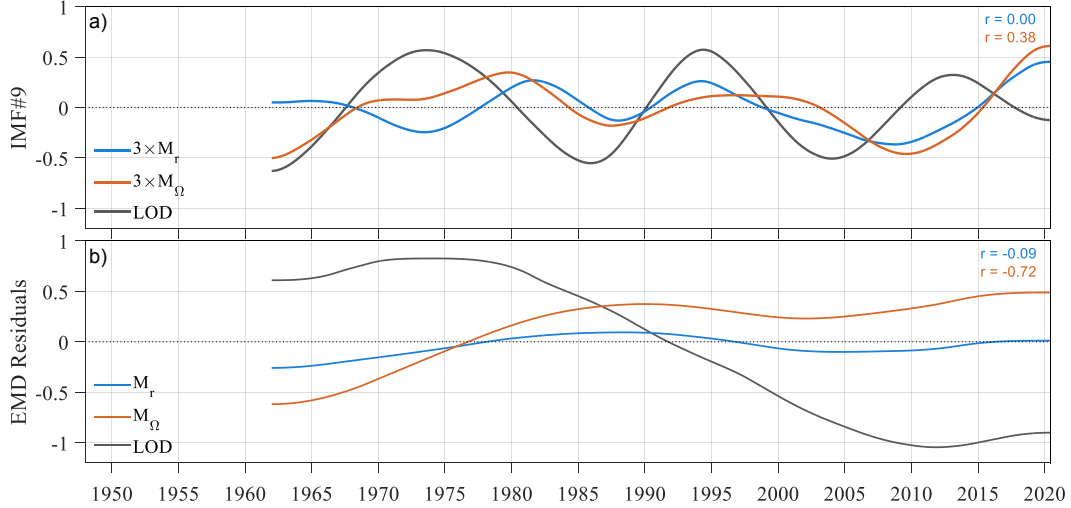


**Figure 4.** Time series plots of (a)  $IMFs\#9$  from Fig. 3 and (b) EMD residuals. Values of  $IMFs\#9$  for  $M_\Omega$  (red lines) and  $M_r$  (blue lines) in (a) are multiplied by a factor of 3 for clarity. Correlation coefficients between  $LOD$  (black lines) and the other two parameters are shown on the top right corners.

### 3.2 Spatio-temporal Variations of AAM

258  
 259 Spatial structures of AAM can be obtained by evaluating the integrals in Eqs. (1)  
 260 and (2) with definite limits for all spatial dimensions (Barnes et al., 1983; Magaña, 1993;  
 261 Abarca del Rio, 1999; Gong et al., 2019). For example, Eqs. (1) and (2) can be integrated  
 262 with respect only to longitude and pressure levels to examine latitudinal variations of  
 263 the AAM. Figures 5(a) and (b) show latitude-time sections of  $M_r(\phi)$  and  $M_\Omega(\phi)$  anoma-  
 264 lies that are calculated as deviations from the climatological (long-term mean) annual-  
 265 cycle. It can be seen that over the equatorial belt, between  $20^\circ\text{S}$  to  $20^\circ\text{N}$ , both  $M_r(\phi)$   
 266 and  $M_\Omega(\phi)$  anomalies show a major change from negative to positive values around the  
 267 1970s. On the contrary, over the southern midlatitude region between  $40^\circ\text{S}$  and  $20^\circ\text{S}$ ,  
 268  $M_r(\phi)$  has changed from dominantly positive to more negative values during the same  
 269 period. In the meantime, the northern midlatitude region between  $40^\circ\text{N}$  to  $20^\circ\text{N}$  shows  
 270 more subtle variations.

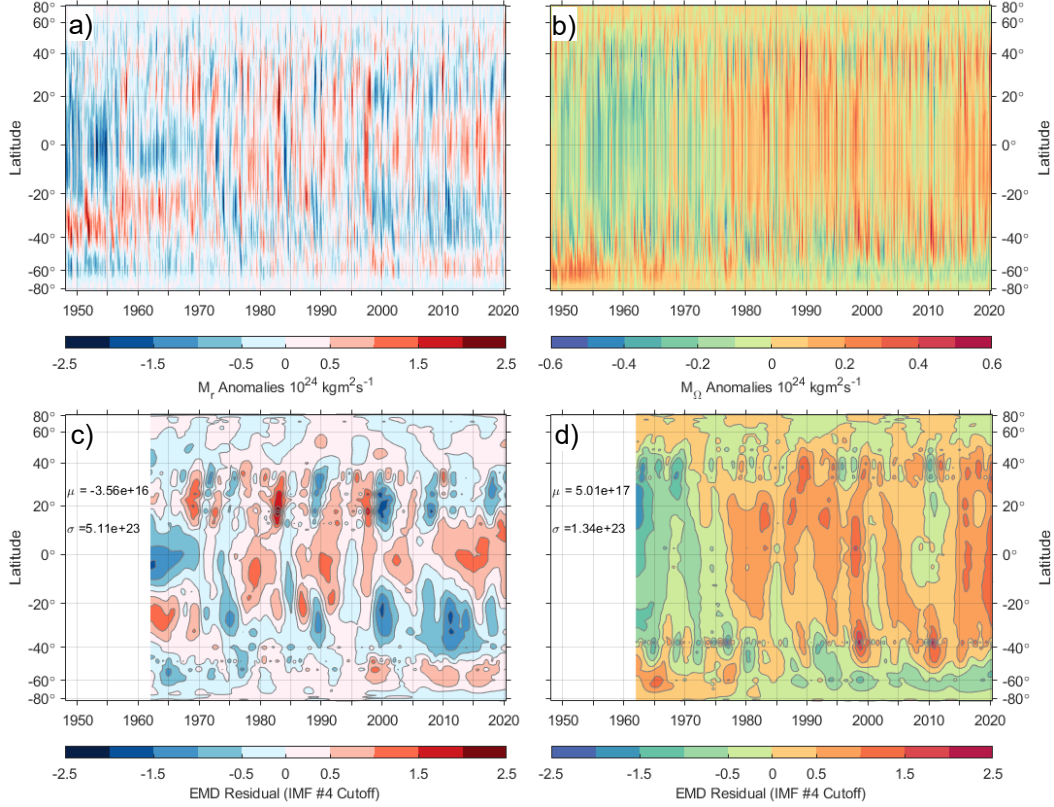


**Figure 5.** Time-latitude sections of (a)  $M_r(\phi)$  anomalies, (b)  $M_\Omega(\phi)$  anomalies, (c) EMD residuals of (a), and (d) EMD residuals of (b). EMD residuals are computed with *IMF#4* cutoff. Values of mean  $\mu$  and standard deviation  $\sigma$  used for normalization (see text) are also shown in (c) and (d). Bivariate EMD analyses are performed against the *LOD* time series so that there is no data before 1962.

271 To emphasize the temporal and latitudinal structures of low-frequency variations,  
 272 we applied bivariate EMD analysis on the  $M_r(\phi)$  and  $M_\Omega(\phi)$  anomalies, shown in Figs.  
 273 5(a) and (b), with respect to *LOD*. In this case, the *LOD* is not deseasonalized so that  
 274 all signals are retained in the time series. It should also be noted that, in this implemen-  
 275 tation of one-dimensional EMD, it is not guaranteed that we can obtain the same max-  
 276 imum number of *IMFs* for each analysis corresponding to each latitude. However, we  
 277 found that all time series can be successfully analyzed against *LOD* up to *IMF#4*. There-  
 278 fore, we use this as a cutoff *IMF* to extract the residuals by Eq. (3) in a manner that  
 279 is similar to low-pass filtering, whose results are shown in Figs. 5(c) and (d).

280 The time-latitude sections of residuals in Figs. 5(c) and (d) more clearly show positive  
 281 trends in both  $M_r$  and  $M_\Omega$  over the equatorial region with patterns of interannual  
 282 variations that are interwoven across latitudes and throughout the observational period.  
 283 Other interesting features can be described as follows:

- 284 1. As expected from Eq. (2), Figs. 5(d) shows that the equatorial region largely con-  
 285 tributes to the changes in  $M_\Omega(\phi)$ . However, there are extensions or even larger  
 286 positive changes in either southern or northern midlatitudes during certain peri-  
 287 ods, such as in the 1990s and most recent decades.
- 288 2. There is a negative long-term trend in  $M_\Omega(\phi)$  anomalies of higher and polar lat-  
 289 itudes of the southern hemisphere, in contrast (but with smaller magnitudes) to  
 290 the positive trend in the equatorial region.
- 291 3. Different from that of  $M_\Omega(\phi)$ , a contrasting pattern of  $M_r(\phi)$  variations are found  
 292 between the equatorial and southern midlatitude regions, especially in those pe-  
 293 riods before 1980 and after 2010.
- 294 4. Episodes of interannual variations in  $M_r(\phi)$  are characterized by propagating pat-  
 295 terns, mainly from the equatorial to mid-latitude regions. For example, marked  
 296 southward (northward) propagation of alternating positive and negative anoma-  
 297 lies in the southern (northern) hemisphere can be seen between 1980 and 1990 (1985  
 298 and 1995).

299 As shown in Fig. 5, we can identify the important contribution of the equatorial  
 300 atmosphere to the variations of global AAM. This view is further augmented by Fig. 6,  
 301 which depicts time-height cross-sections of global (Fig. 6(a)) and equatorial (Fig. 6(c))  
 302  $M_r$  anomalies with similar patterns of spatio-temporal variations. In the upper tropo-  
 303 sphere and lower stratosphere (UTLS), the equatorial QBO dominates although the con-  
 304 tribution to the total AAM is limited because of the low density. Through the tropo-  
 305 sphere, on the other hand, vertically coherent interannual variation prevails with large  
 306 contribution of the equatorial region. As in Fig. 5, herein, we apply bivariate EMD anal-  
 307 ysis on  $M_r(p)$  and  $LOD$  to obtain the residuals, with  $IMF\#4$  cutoff, in each pressure  
 308 level, and show them in Figs. 6(b) and (d) for global and equatorial regions, respectively.  
 309 By visual comparisons, the vertical structure of global  $M_r(p)$  anomalies is largely char-  
 310 acterized by the variations in the equatorial region. In addition, we delineate three lay-  
 311 ers where  $M_r(p)$  variations are significantly different, i.e., the lower troposphere (1000

312 to 700 hPa), the mid and upper troposphere (700 to 250 hPa), and UTLS (250 to 10 hPa).  
 313 By focusing on the low-frequency variations of equatorial  $M_r(p)$  in Figs. 6(d), tempo-  
 314 ral structures in these three layers can be described as follows:

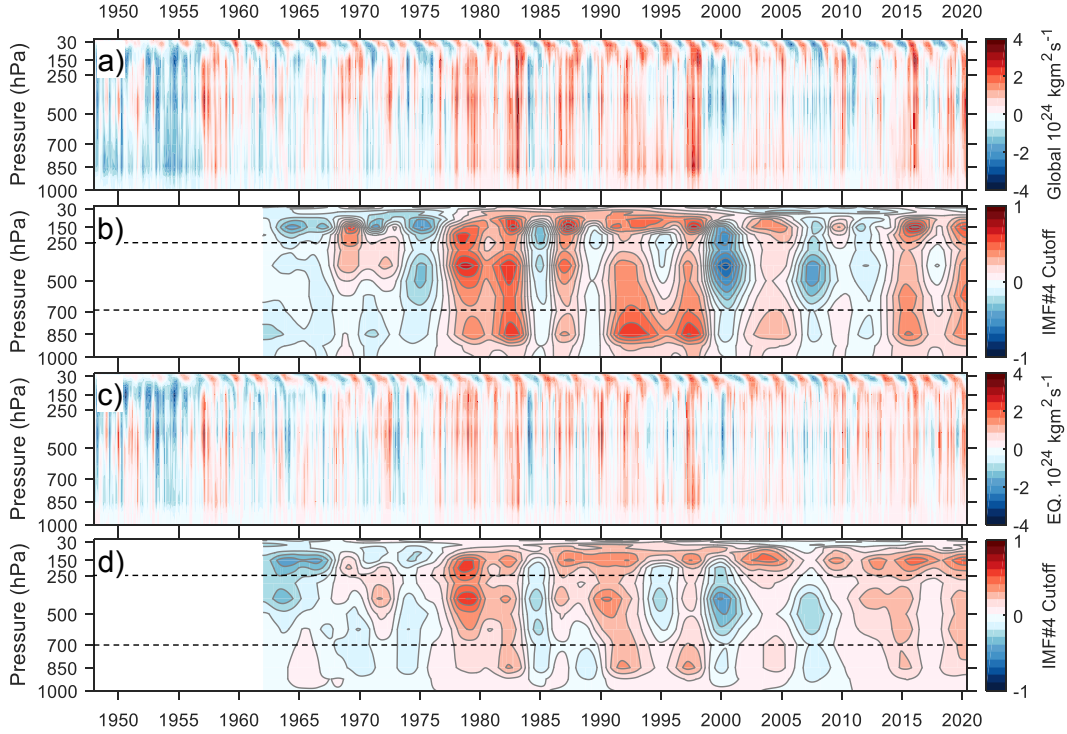


**Figure 6.** Similar to Fig. 5 but for time-vertical sections of  $M_r(p)$ : (a) global (pole-to-pole) anomalies, (b) EMD residuals of (a), (c) equatorial (20°S to 20°N) anomalies, and (d) EMD residuals of (c). Data for EMD analyses are normalized using  $\sigma$  in Fig. 5(c) as a common denominator, whereas mean values are computed and subtracted to the time series for each layer. Horizontal black dashed lines mark three divisions of vertical layers, which are further analyzed in Fig 7.

- 315 1. Overall,  $M_r(p)$  anomalies have drastically changed from predominantly negative
- 316 before the mid 1970s to mostly positive in all layers after 2010.
- 317 2. In UTLS,  $M_r(p)$  anomalies are characterized with one major change from dom-
- 318 inantly negative to dominantly positive values in the mid-1970s.
- 319 3. In the mid and upper troposphere layer, more significant positive and negative vari-
- 320 ations of  $M_r(p)$  occurred between 1975 to 2010, transitioning into a deep layer of
- 321 positive anomalies that are more pronounced in the last decade.
- 322 4. In the lower troposphere layer,  $M_r(p)$  variations are characterized by alternating
- 323 in- and out-of-phase changes with respect to those in the middle and upper tro-

324 posphere before 2000; since then, these variations have been more consistently in-  
 325 phase.

### 326 3.3 Low-Frequency Variations of Equatorial AAM

327 It is still difficult to see whether these changes are vertically propagating downward  
 328 or upward from the previously mentioned results. However, it is interesting to examine  
 329 further the correlations among low-frequency variations of equatorial  $M_r$  in the previ-  
 330 ously mentioned three layers and  $LOD$ . Therefore, we again apply bivariate EMD anal-  
 331 ysis between layer-averaged  $M_r$  and  $LOD$  and plotted the residuals, but with  $IMF\#6$   
 332 cutoff, in Fig. 7. It can be seen that in these residuals,  $LOD$  variations are character-  
 333 ized by a three-peak pattern that occurred around the 1970s, 1990s, and 2010s, super-  
 334 imposed on a long-term negative trend. On the other hand,  $M_r$  variations differ from  
 335 one layer to the other with a less discernible positive trend except in UTLS (Fig. 7(a)).

336 In Fig. 7, we also calculated and plotted Earth's acceleration (black dashed lines),  
 337 which is simply defined as the negative time derivative of  $LOD$  residuals (black lines),  
 338 i.e.,

$$\dot{\Lambda} = -\frac{d\Re_{LOD}}{dt} \quad (4)$$

339 If  $LOD$  excitation is associated with atmospheric variations,  $\dot{\Lambda}$  should be proportional  
 340 to the rate of change of AAM, which also means proportional to total torques that are  
 341 mainly contributed by the frictional and mountain torques (Gong et al., 2019). All-time  
 342 correlation coefficients between  $M_r$  and normalized  $\dot{\Lambda}$  is more than 0.4 in the lower tro-  
 343 posphere, whereas those in the other two layers are around 0.3. Computed 20-year slid-  
 344 ing correlation coefficients (shown as bar charts) confirm that low-frequency variations  
 345 of  $M_r$  in the lower troposphere are more consistently in phase with  $\dot{\Lambda}$ . In contrast, changes  
 346 in the sign of the sliding correlations occur in other layers. These results indicate that  
 347 more direct interactions between Earth's rotation and AAM occur in the equatorial lower  
 348 troposphere.

### 349 3.4 Long-term Trend of Equatorial AAM

350 In the previous subsections, we have shown that EMD residuals can be regarded  
 351 as low-pass filtered time series when cutoff  $IMF$  number is not the maximum; other-  
 352 wise, residuals are more associated with trends (Wu et al., 2007). As shown in Fig. 4(b),

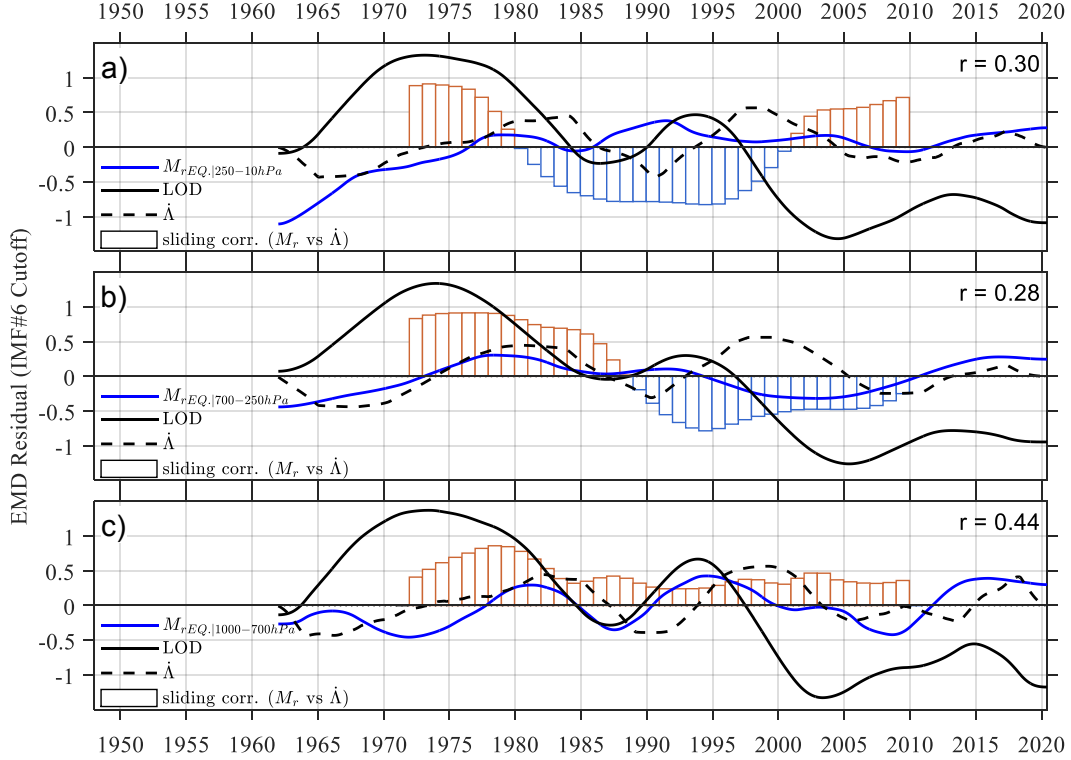


**Figure 7.** Bivariate EMD residuals with *IMF#6* cutoff of *LOD* (solid black lines) and equatorial  $M_r$  (blue lines) averaged in three layers (see Fig. 6): (a)UTLS (250 - 10 hPa),(b)middle and upper-troposphere, and (c)lower troposphere (1000 - 700 hPa). Black dashed lines denote normalized Earth acceleration  $\dot{\Lambda}$  defined by equation (4), whereas bar charts depict the coefficients of 20-year sliding correlation between  $M_r$  and  $\dot{\Lambda}$  (see text).

353 the long-term trend in *LOD* is correlated with globally integrated  $M_\Omega$  rather than  $M_r$ .  
 354 However, since  $M_\Omega$  is contributed mainly by the equatorial region, we analyzed the trends  
 355 by focusing on the equatorial atmosphere. The residuals of *LOD* along with  $\dot{\Lambda}$ ,  $M_\Omega$ , and  
 356 lower tropospheric  $M_r$  are shown in Fig. 8. It can be seen that a large portion of the *LOD*  
 357 time series is monotonically decreasing from around 1980 to around 2010, which is neg-  
 358 atively correlated with the long-term trend of  $M_\Omega$  and  $M_r$  over the equatorial region.  
 359 Although there are still some undulating components in the time series, acceleration in  
 360 the Earth’s rotation during 1970s to 2000 is associated with an increase in  $M_\Omega$  and lower  
 361 tropospheric  $M_r$  over the equatorial region.

362 Although the values of  $M_\Omega$  are determined mainly by surface pressure over the equa-  
 363 torial belt, Fig. 5(d) indicates that there are also temporal variations in midlatitude and

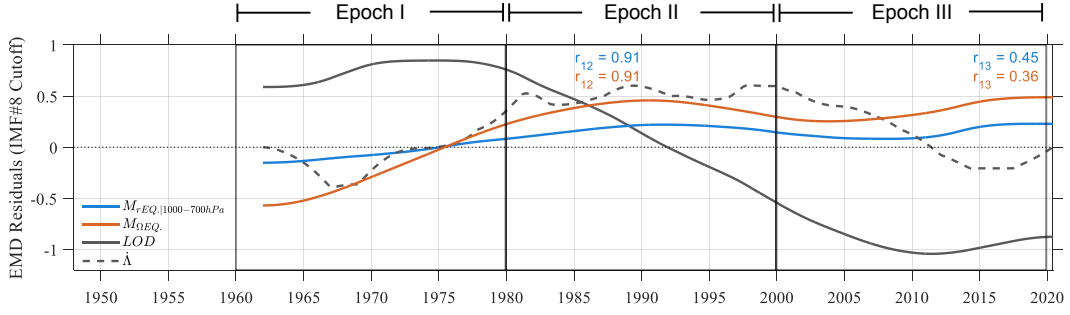


**Figure 8.** Similar to Fig 4 but for EMD residuals with the largest *IMF#8* cutoff showing trends of equatorial lower tropospheric  $M_r$  (blue line),  $M_\Omega$  (red line), and  $LOD$  (solid black line), as well as normalized  $\dot{\Lambda}$  (black dashed line). The data period is divided into three 20-year epochs, as indicated on the top.

364 polar regions. To see the horizontal structures of the trends, we divide the data period  
 365 into three 20-year epochs as indicated on the top of Fig. 8 and plotted the differences  
 366 in  $M_\Omega(\phi, \lambda)$  and lower tropospheric  $M_r(\phi, \lambda)$  between two consecutive epochs as colored  
 367 contour maps in Fig. 9. It can be seen that between the first two epochs,  $M_\Omega(\phi, \lambda)$  had  
 368 almost uniformly increased over the entire equatorial belt, especially over the African  
 369 and Asian Continents. An increase in  $M_\Omega(\phi, \lambda)$  can also be observed over the Maritime  
 370 Continent and Indian Ocean, whereas the trends in midlatitude regions over the Pacific  
 371 Ocean are mainly negative. Furthermore, the southern polar region is markedly char-  
 372 acterized by negative trends. These trends are largely reversed between the third and  
 373 second epochs except over the Central Pacific and southern polar region. The magni-  
 374 tude of negative trends between the last two epochs is, in general, weaker compared to  
 375 the preceding positive trends, but a relatively large decrease in  $M_\Omega(\phi, \lambda)$  is observed over  
 376 the Maritime Continent.

377 Change of signs also characterizes the trends in lower tropospheric  $M_r(\phi, \lambda)$  but  
 378 with more significant zonal variations along the equatorial belt. Positive trends between  
 379 the first two epochs mainly occurred over the Pacific Ocean and South America, with  
 380 contrasting negative trends over the Atlantic Ocean and Africa. This pattern is some-  
 381 what reversed from the second and third epochs, with positive trends over the Atlantic  
 382 Ocean. However, while trends over the Pacific Ocean become negative, positive trends  
 383 still prevail over the eastern Pacific and South America. Persistent positive trends are

384 also observed over the southern polar region and western part of the Maritime Conti-  
 385 nent.

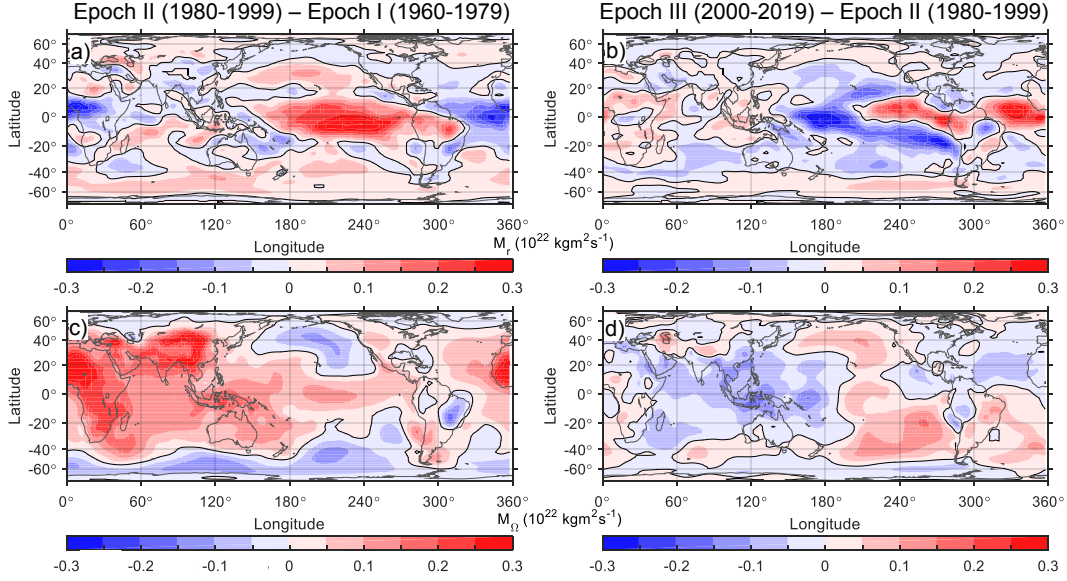


**Figure 9.** Spatial variations of trends in  $M_r(\phi, \lambda)$  (upper panels) and  $M_\Omega(\phi, \lambda)$  (lower panels) calculated as differences in mean values between two consecutive epochs defined in Fig. 8.

#### 386 4 Discussions

387 Our results of EMD analyses strongly indicate that the increase in Earth’s rota-  
 388 tion rate during the last five decades can be associated with an increase in both  $M_\Omega$  and  
 389 lower tropospheric  $M_r$  over the equatorial belt (Fig. 8). The long-term trend of equa-  
 390 torial  $M_\Omega$  is similar to that of the global domain (Fig. 5 (b)), which is negatively cor-  
 391 related with  $LOD$  and indicates the important role of equatorial region. Although tran-  
 392 sient phenomena like MJO and ENSO may have residual effects at longer times (Huang  
 393 et al., 2001; Lee, 1999), which could be manifested as low-frequency oscillatory variations  
 394 in Fig. 7, our results are more suggestive that the long-term positive trend in  $M_\Omega$  found  
 395 in Fig. 8 was mainly forced by the global increase of surface pressure as indicated by Fig.  
 396 9(c). The period around the mid-1970s, during which  $M_\Omega$  have significantly increased,  
 397 is widely known as the period of global climate shift event (e.g., Meehl et al., 2009). The  
 398 positive trend is more relaxed afterward, but the global increase of surface pressure dur-  
 399 ing the 1970s seems to have a prolonged effect on the equatorial  $M_\Omega$ .

400 Variations of  $M_r$  and  $M_\Omega$  are, on average, tend to be positively correlated at inter-  
 401 terannual and longer time scales (Fig. 3). However, positive correlation between  $M_r$  and  
 402  $M_\Omega$  only prevails over the equatorial region, whereas negative correlation is more pre-  
 403 dominant over mid- and high-latitude regions (Figs. 5(c) and (d)). The negative corre-  
 404 lation between  $M_r$  and  $M_\Omega$  reflects the AAM conservation and, on the contrary, posi-  
 405 tive correlation implies residual changes due to acting torques. The increase in equato-  
 406 rial lower-tropospheric  $M_r$  should correspond to weaker easterlies, which is explicable  
 407 by a larger transfer of eastward momentum to the atmosphere due to accelerating Earth  
 408 (Figs. 7 and 9) but globally integrated  $M_r$  shows almost negligibly small long-term trend  
 409 (Fig. 4). This indicates that spatio-temporal redistribution of  $M_r$  anomalies tends to bal-  
 410 ance residual changes in the equatorial atmosphere. Figure 5 shows that  $M_r(\phi)$  anoma-  
 411 lies tend to be dominantly negative in midlatitude regions during recent decades, while  
 412 positive anomalies are stronger near the southern hemispheric polar region. However,  
 413 this condition is almost the opposite of what has been observed before the mid-1970s,  
 414 and poleward propagation of  $M_r(\phi)$  anomalies can be identified in the interannual vari-  
 415 ations. Herein, we do not discuss pathways of spatial redistribution of the equatorial  $M_r(\phi)$   
 416 anomalies in further detail. Among other possibilities, Huang et al. (2003) have stud-  
 417 ied the transient  $M_r$  variations associated with 1965 and 1972 El Niños and Salstein (2015)  
 418 pointed out that poleward propagation of ENSO induced AAM anomalies has been iden-  
 419 tified in previous studies.

420 A long-lasting change in  $M_\Omega$  might lead to an important impact on the Earth's cli-  
 421 mate system. In this regard, we have shown a possible connection between  $M_\Omega$  and  $LOD$ ,  
 422 but various Earth-bound and solar-terrestrial processes, including global warming, could  
 423 be attributable to multidecadal variations in  $LOD$  and AAM either dependently or inter-  
 424 dependently. However, ocean-atmosphere interactions play major roles in long-term cli-  
 425 matic processes. Fig. 9 shows that the multidecadal trends in  $M_r(\phi, \lambda)$  exhibit strong  
 426 zonal variations, indicating different roles of oceans and continents in the momentum trans-  
 427 fers along the equatorial region. Considering that the dynamical system of the oceans  
 428 has longer memory compared to that of the atmosphere, it is quite intuitive to exam-  
 429 ine correlations between  $LOD$  and oceanic climate indices as presented in Fig. 10, where  
 430 we have chosen three indices to compare with  $LOD$ , i.e., Nino34 (ENSO), DMI (Dipole  
 431 Mode Index), and AMO (Atlantic Multi-decadal Oscillation) index representing oceanic  
 432 climate variabilities in the Pacific Ocean, Indian Ocean, and the Atlantic Ocean. In ad-

433 condition, GMI (Geomagnetic Ap index) that represents the non-atmospheric/oceanic com-  
 434 ponent is also analyzed. Wahr (1988) pointed out that changes in the Earth's rotation  
 435 due to electromagnetic forcing are viable.

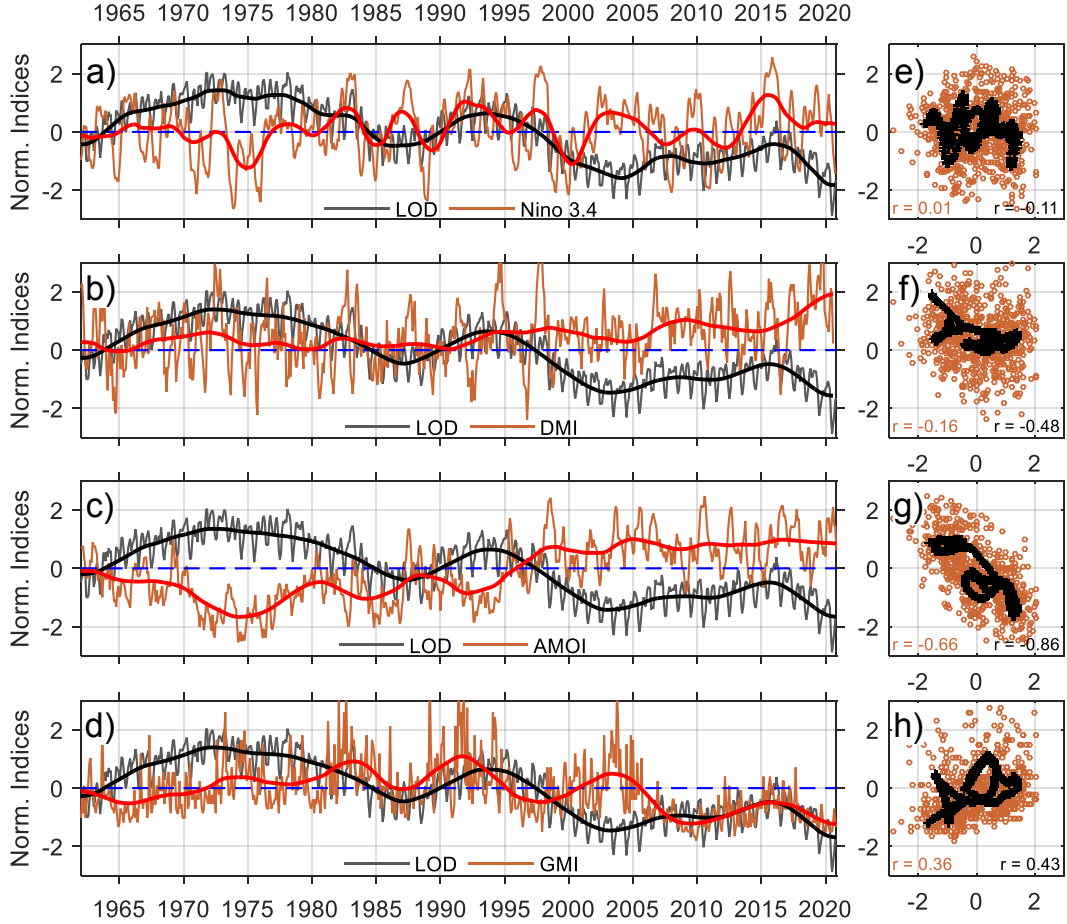


**Figure 10.** Correlations between *LOD* (black lines) and three oceanic climate indices, i.e., Nino34, DMI, AMO index, and geomagnetic (*Ap*) index (red lines) presented in the form of time series (left panels) and scatter plots (right panels). Thick lines on the left panels are smoothed values obtained as bivariate EMD residuals with subjectively chosen *IMF#* cutoff. For the scatter plots, red circles and black plus marks correspond to monthly (raw) and smoothed data, respectively. Correlation coefficients are also shown in the scatter plots.

436 Among four analyzed indices, it is clear from Fig. 10 that AMO has the strongest  
 437 linear correlation with *LOD*. Even for monthly time series, the correlation between AMO  
 438 index and *LOD* is around -0.7 and close to -0.9 for the smoothed data. This result some-  
 439 what differs from that of Marcus (2016), who found that *LOD* has a stronger correla-

440 tion with global mean SST than AMO. It is probably also noteworthy that Fig. 10 shows  
 441 higher negative (positive) correlations between  $LOD$  and DMI (GMI) compared to that  
 442 of  $LOD$  and Nino34. Detailed processes that link AMO and other climate indicators with  
 443  $LOD$  variations are beyond the scope of this study. Nonetheless, we can point out that  
 444 the Earth's rotation rate is closely related to atmospheric and oceanic variations that  
 445 define climate conditions at decadal and longer time scales.

## 446 5 Conclusions

447 We have analyzed the low-frequency variability of AAM by applying the bivariate  
 448 and trivariate EMD method to extract coherent nonstationary signals from the monthly  
 449 time series of  $LOD$ ,  $M_\Omega$ , and  $M_r$ , as well as climate indices. We have found that, over  
 450 the global domain, the decreasing trend of  $LOD$  during the last five decades is correlated  
 451 with an increasing trend in  $M_\Omega$ , whereas the trend in  $M_r$  is negligible.

452 The long-term positive trend in  $M_\Omega$  is most likely attributed to a global increase  
 453 in surface pressure from the mid-1970s until about 1990, which seems to have profoundly  
 454 affected the atmosphere-ocean dynamical systems over the equatorial belt for a prolonged  
 455 duration. There is a significant positive trend in  $M_r$  of the equatorial lower troposphere  
 456 (from 1000 to 700 hPa), which is consistent with a larger transfer of eastward momen-  
 457 tum due to accelerating Earth. However, a slight long-term trend in globally integrated  
 458  $M_r$  and spatio-temporal variations of  $M_r$  suggest a redistribution of  $M_r$  anomalies across  
 459 the globe by climate processes at interannual to multidecadal time scales.

460 Although we do not specifically investigate the primary source of low-frequency  $LOD$   
 461 variations, a comparison between the time series of  $LOD$  and the AMO index shows a  
 462 high correlation coefficient value. Furthermore, we have inferred that two-way interac-  
 463 tions between Earth rotation and AAM at a multidecadal time scale are plausible so that  
 464 changes in Earth's rotation rate are (at least) partially attributable to low-frequency oceanic  
 465 and atmospheric variability and vice versa. Thus, incorporating a feedback mechanism  
 466 of  $LOD$  variations might need to be considered in future development of global climate  
 467 models to accurately describe the angular momentum transfer between the solid Earth  
 468 and the atmosphere and oceans.

469 **Acknowledgments**

470 This research was mainly supported by JSPS-DGHE of The Indonesian Ministry for Ed-  
 471 ucation, Culture, Research, and Technology Joint Research Project FY 2020. The first  
 472 and second authors (TWH and FRF) are also partially supported by ITB-P3MI Research  
 473 Grant FY 2021.

474 **References**

- 475 Abarca del Rio, R. (1999). The influence of global warming in earth rotation speed.  
 476 *Annales Geophysicae*, *17*(6), 806–811. doi: 10.1007/s00585-999-0806-x
- 477 Abarca-del Rio, R., Gambis, D., & Salstein, D. (2000, 03). Interannual signals in  
 478 length of day and atmospheric angular momentum. *Annales Geophysicae*, *18*,  
 479 347-364. doi: 10.1007/s00585-000-0347-9
- 480 Aoyama, Y., & Naito, I. (2000). Wind contributions to the earth’s angular mo-  
 481 mentum budgets in seasonal variation. *Journal of Geophysical Research: Atmo-*  
 482 *spheres*, *105*(D10), 12417-12431. doi: 10.1029/2000JD900101
- 483 Barlyaeva, T., Bard, E., & Abarca-del Rio, R. (2014). Rotation of the earth, solar  
 484 activity and cosmic ray intensity. *Annales Geophysicae*, *32*(7), 761–771. doi:  
 485 10.5194/angeo-32-761-2014
- 486 Barnes, R. T. H., Hide, R., White, A. A., & Wilson, C. A. (1983). Atmospheric  
 487 angular momentum fluctuations, length-of-day changes and polar motion. *Pro-*  
 488 *ceedings of the Royal Society of London. Series A, Mathematical and Physical*  
 489 *Sciences*, *387*(1792), 31–73.
- 490 Birner, T., Davis, S. M., & Seidel, D. J. (2014). The changing width of earth’s tropi-  
 491 cal belt. *Physics Today*, *67*(12), 38-44. doi: 10.1063/PT.3.2620
- 492 Bizouard, C., Lambert, S., Gattano, C., Becker, O., & Richard, J.-Y. (2019, 08).  
 493 The iers eop 14c04 solution for earth orientation parameters consistent with  
 494 itrf 2014. *Journal of Geodesy*, *93*, 621–633. doi: 10.1007/s00190-018-1186-3
- 495 Davis, S. M., & Rosenlof, K. H. (2012). A multidiagnostic intercomparison of  
 496 tropical-width time series using reanalyses and satellite observations. *Journal*  
 497 *of Climate*, *25*(4), 1061 - 1078. doi: 10.1175/JCLI-D-11-00127.1
- 498 Duhau, S. (2006). Solar activity, earth’s rotation rate and climate variations in  
 499 the secular and semi-secular time scales. *Physics and Chemistry of the Earth,*  
 500 *Parts A/B/C*, *31*(1), 99 - 108. (Long Term Changes and Trends in the Atmo-

- 501 sphere) doi: 10.1016/j.pce.2005.03.006
- 502 Egger, J., & Hoinka, K.-P. (2005). The annual cycle of the axial angular momentum  
503 of the atmosphere. *Journal of Climate*, 18(6), 757 - 771. doi: 10.1175/JCLI  
504 -3290.1
- 505 Egger, J., Weickmann, K., & Hoinka, K.-P. (2007). Angular momentum in the  
506 global atmospheric circulation. *Reviews of Geophysics*, 45(4). doi: 10.1029/  
507 2006RG000213
- 508 Fajary, F. R., Hadi, T. W., & Yoden, S. (2019). Contributing factors to spatiotem-  
509 poral variations of outgoing longwave radiation (olr) in the tropics. *Journal of*  
510 *Climate*, 32(15), 4621 - 4640. doi: 10.1175/JCLI-D-18-0350.1
- 511 Feldstein, S. B. (1999). The atmospheric dynamics of intraseasonal length-of-day  
512 fluctuations during the austral winter. *Journal of the Atmospheric Sciences*,  
513 56(17), 3043 - 3058. doi: 10.1175/1520-0469(1999)056<3043:TADOIL>2.0.CO;  
514 2
- 515 Fujiwara, M., Wright, J. S., Manney, G. L., Gray, L. J., Anstey, J., Birner, T., ...  
516 Zou, C.-Z. (2017). Introduction to the sparc reanalysis intercomparison  
517 project (s-rip) and overview of the reanalysis systems. *Atmospheric Chemistry*  
518 *and Physics*, 17(2), 1417–1452. doi: 10.5194/acp-17-1417-2017
- 519 Gong, H., Huang, M., Zhu, L., & Shao, Y. (2019). Long-term variations of atmo-  
520 spheric angular momentum and torque. *Meteorology and Atmospheric Physics*,  
521 1-15.
- 522 Grimes, A. (1951). Equatorial meteorology. In T. F. Malone (Ed.), *Compendium of*  
523 *meteorology: Prepared under the direction of the committee on the compendium*  
524 *of meteorology* (pp. 881–886). Boston, MA: American Meteorological Society.  
525 doi: 10.1007/978-1-940033-70-9\_71
- 526 Huang, H.-P., Weickmann, K. M., & Hsu, C. J. (2001). Trend in atmospheric  
527 angular momentum in a transient climate change simulation with green-  
528 house gas and aerosol forcing. *Journal of Climate*, 14(7), 1525 - 1534. doi:  
529 10.1175/1520-0442(2001)014<1525:TIAAMI>2.0.CO;2
- 530 Huang, H.-P., Weickmann, K. M., & Rosen, R. (2003). Unusual behavior in atmo-  
531 spheric angular momentum during the 1965 and 1972 el niños. *Journal of Cli-*  
532 *mate*, 16, 2526-2539.
- 533 IERS Earth Orientation Centre. (2020). *EOP 14 C04 series for 1962-continuing*.

- 534 [dataset]. IERS Earth Orientation Centre. Retrieved from [https://](https://datacenter.iers.org/data/223/eopc04_14.62-now.txt)  
 535 [datacenter.iers.org/data/223/eopc04\\_14.62-now.txt](https://datacenter.iers.org/data/223/eopc04_14.62-now.txt) (Update frequency:  
 536 bi-weekly)
- 537 Kalnay, E., Kanamitsu, M., Kistler, R., Collins, W., Deaven, D., Gandin, L.,  
 538 ... Joseph, D. (1996). The NCEP/NCAR 40-Year Reanalysis Project.  
 539 *Bulletin of the American Meteorological Society*, *77*(3), 437 - 472. doi:  
 540 10.1175/1520-0477(1996)077<0437:TNYRP>2.0.CO;2
- 541 Lambeck, K., & Hopgood, P. (1982, 12). The earth's rotation and atmospheric circu-  
 542 lation: 1958-1980. *Geophysical Journal International*, *71*(3), 581-587. doi: 10  
 543 .1111/j.1365-246X.1982.tb02785.x
- 544 Lee, S. (1999). Why are the climatological zonal winds easterly in the equatorial up-  
 545 per troposphere? *Journal of the Atmospheric Sciences*, *56*(10), 1353 - 1363.  
 546 doi: 10.1175/1520-0469(1999)056<1353:WATCZW>2.0.CO;2
- 547 Madden, R. A. (1987). Relationships between changes in the length of day and the  
 548 40- to 50- day oscillation in the tropics. *Journal of Geophysical Research: At-*  
 549 *mospheres*, *92*(D7), 8391-8399. doi: 10.1029/JD092iD07p08391
- 550 Magaña, V. (1993). The 40- and 50-day oscillations in atmospheric angular mo-  
 551 mentum at various latitudes. *Journal of Geophysical Research: Atmospheres*,  
 552 *98*(D6), 10441-10450. doi: 10.1029/93JD00343
- 553 Marcus, S. (2016). Does an intrinsic source generate a shared low-frequency signa-  
 554 ture in earth's climate and rotation rate? *Earth Interactions*, *20*, 1-14.
- 555 Match, A., & Fueglistaler, S. (2019). The buffer zone of the quasi-biennial oscilla-  
 556 tion. *Journals of the Atmospheric Sciences*, *76*(11), 3553-3567. doi: 10.1175/  
 557 JAS-D-19-0151.1
- 558 Meehl, G., Hu, A., & Santer, B. (2009). The mid-1970s climate shift in the pacific  
 559 and the relative roles of forced versus inherent decadal variability. *Journal of*  
 560 *Climate*, *22*, 780-792.
- 561 NCEP/NWS/NOAA/U.S. Department of Commerce. (1994). *NCEP/NCAR Global*  
 562 *Reanalysis Products, 1948-continuing*. [dataset]. NOAA/ESRL/PSL. Retrieved  
 563 from <https://psl.noaa.gov/data/gridded/data.ncep.reanalysis.html>
- 564 Oort, A. H. (1989). Angular momentum cycle in the atmosphere?ocean?solid earth  
 565 system. *Bulletin of the American Meteorological Society*, *70*(10), 1231 - 1242.  
 566 doi: 10.1175/1520-0477(1989)070<1231:AMCITA>2.0.CO;2

- 567 Paek, H., & Huang, H.-P. (2012). A comparison of the interannual variability in  
 568 atmospheric angular momentum and length-of-day using multiple reanalysis  
 569 data sets. *Journal of Geophysical Research: Atmospheres*, *117*(D20). doi:  
 570 10.1029/2012JD018105
- 571 PSL/NOAA. (2020). *Climate Indices*. PSL/NOAA. Retrieved from [https://psl](https://psl.noaa.gov/data/climateindices/)  
 572 [.noaa.gov/data/climateindices/](https://psl.noaa.gov/data/climateindices/) (Data collected from various sources)
- 573 Salstein, D. A. (2015). General circulation of the atmosphere — angular momentum  
 574 of the atmosphere. In G. R. North, J. Pyle, & F. Zhang (Eds.), *Encyclope-*  
 575 *dia of atmospheric sciences (second edition)* (Second Edition ed., p. 43-50).  
 576 Oxford: Academic Press. doi: 10.1016/B978-0-12-382225-3.00043-8
- 577 Salstein, D. A., Kann, D. M., Miller, A. J., & Rosen, R. D. (1993). The sub-bureau  
 578 for atmospheric angular momentum of the international earth rotation ser-  
 579 vice: A meteorological data center with geodetic applications. *Bulletin of the*  
 580 *American Meteorological Society*, *74*(1), 67–80.
- 581 Starr, V. P. (1948). An essay on the general circulation of the earth's atmosphere.  
 582 *Journal of Atmospheric Sciences*, *5*(2), 39 - 43. doi: 10.1175/1520-0469(1948)  
 583 005(0039:AEOTGC)2.0.CO;2
- 584 Thirumalaisamy, M. (2020, July). *Fast and adaptive multivariate and mul-*  
 585 *tidimensional emd*. Retrieved from [https://www.mathworks.com/](https://www.mathworks.com/matlabcentral/fileexchange/71270-fast-and-adaptive-multivariate-and-multidimensional-emd)  
 586 [matlabcentral/fileexchange/71270-fast-and-adaptive-multivariate](https://www.mathworks.com/matlabcentral/fileexchange/71270-fast-and-adaptive-multivariate-and-multidimensional-emd)  
 587 [-and-multidimensional-emd](https://www.mathworks.com/matlabcentral/fileexchange/71270-fast-and-adaptive-multivariate-and-multidimensional-emd) (MATLAB Central File Exchange)
- 588 Thirumalaisamy, M. R., & Ansell, P. J. (2018, Oct). Fast and adaptive empiri-  
 589 cal mode decomposition for multidimensional, multivariate signals. *IEEE Sig-*  
 590 *nal Processing Letters*, *25*(10), 1550-1554. doi: 10.1109/LSP.2018.2867335
- 591 Wahr, J. M. (1988). The earth's rotation. *Annual Review of Earth and Planetary*  
 592 *Sciences*, *16*(1), 231-249. doi: 10.1146/annurev.ea.16.050188.001311
- 593 Weickmann, K. M., & Sardeshmukh, P. D. (1994). The atmospheric angular mo-  
 594 mentum cycle associated with a madden-julian oscillation. *Journal of Atmo-*  
 595 *spheric Sciences*, *51*(21), 3194 - 3208. doi: 10.1175/1520-0469(1994)051(3194:  
 596 TAAMCA)2.0.CO;2
- 597 Wu, Z., Feng, J., Qiao, F., & Tan, Z.-M. (2016). Fast multidimensional ensemble  
 598 empirical mode decomposition for the analysis of big spatio-temporal datasets.  
 599 *Philosophical Transactions of the Royal Society A: Mathematical, Physical and*

- 600            *Engineering Sciences*, 374(2065), 20150197. doi: 10.1098/rsta.2015.0197
- 601        Wu, Z., Huang, N. E., Long, S. R., & Peng, C.-K. (2007). On the trend, detrend-  
602            ing, and variability of nonlinear and nonstationary time series. *Proceedings of*  
603            *the National Academy of Sciences*, 104(38), 14889–14894. doi: 10.1073/pnas  
604            .0701020104
- 605        Zotov, L., Bizouard, C., & Shum, C. (2016). A possible interrelation between earth  
606            rotation and climatic variability at decadal time-scale. *Geodesy and Geodynam-*  
607            *ics*, 7(3), 216-222. (Special Issue: Geodetic and Geophysical Observations and  
608            Applications and Implications) doi: 10.1016/j.geog.2016.05.005